Martín Díaz, J.; Arnau Martínez, FJ.; Piqueras Cabrera, P.; Auñón García, Á. (2018). Development of an Integrated Virtual Engine Model to Simulate New Standard Testing Cycles. SAE Technical Papers. doi:10.4271/2018-01-1413

# Development of an Integrated Virtual Engine Model to Simulate New Standard Testing Cycles

**Jaime Martín, Francisco Arnau, Pedro Piqueras and Angel Auñón**
Universitat Politècnica de València

## Abstract

The combination of more strict regulation for pollutant and $CO_2$ emissions and the new testing cycles, covering a wider range of transient conditions, makes very interesting the development of predictive tools for engine design and pre-calibration. This paper describes a new integrated Virtual Engine Model (VEMOD) that has been developed as a standalone tool to simulate new standard testing cycles. The VEMOD is based on a wave-action model that carries out the thermo-and fluid dynamics calculation of the gas in each part of the engine. In the model, the engine is represented by means of 1D ducts, while the volumes, such as cylinders and reservoirs, are considered as 0D elements. Different sub-models are included in the VEMOD to take into account all the relevant phenomena. Thus, the combustion process is calculated by the Apparent Combustion Time (ACT) 1D model, responsible for the prediction of the rate of heat release and $NO_x$ formation. Experimental correlations are used to determine the rest of pollutants. In order to predict tailpipe pollutant emissions to the ambient, different sub-models have been developed to reproduce the behavior of the aftertreatment devices (DOC and DPF) placed in the exhaust system. Dedicated friction and auxiliaries sub-models allow obtaining the brake power. The turbocharger consists of 0D compressor and turbine sub-models capable of extrapolating the available maps of both devices. The VEMOD includes coolant and lubricant circuits linked, on the one hand, with the engine block and the turbocharger through heat transfer lumped models; and on the other hand with the engine heat exchangers. A control system emulating the ECU along with vehicle and driver sub-models allow completing the engine simulation. The Virtual Engine Model has been validated with experimental tests in a 1.6 L Diesel engine using steady and transient tests in both hot and cold conditions. Engine torque was predicted with a mean error of 3 Nm and an error below 14 Nm for 90 % of the cycle duration. $CO_2$ presented a mean error of 0.04 g/s, while during 80 % of the cycle, error was below 0.44 g/s.

## Introduction

The increasingly stringent government mandates on fuel economy and $CO_2$ emissions reduction have led to a new way to determine passenger car emissions called World harmonized Light vehicles Test Procedure (WLTP)[1], which has come into force in September 2017 in Euro 6d-Temp, which is also including Real Driving Emission tests. The assessment of emissions will be completed defining this new framework with extended ambient temperature ranges covering very cold conditions as well as the altitude effect.

This new paradigm has pushed the automotive industry to the widespread adoption of IC Engine rightsizing, turbocharging, direct injection and flexible valve actuation technology as a standard solution for fuel economy improvement of passenger cars and light-duty trucks [2], not only in CI engines, which have been using these technologies for long time, but also nowadays in SI engines. Such evolution in the engine design has significantly increased the complexity of the air path system, particularly introducing a large number of degrees of freedom to control the cylinder charge, as well as its thermodynamic condition and composition.

This paper presents a virtual engine model based on a wave-action 1D model able to simulate new standard testing cycles. Even though VEMOD has been validated in a 1.6L Diesel engine most of its sub-models are also suitable for petrol engines (air path, mechanical losses, hydraulic circuits…). Hence, in its actual state there is only one main limitation that is the combustion and NOx models that are physically based taking into account the CI phenomena. Future model upgrades will include this possibility for SI engines.

Some of the VEMOD sub-models were separately developed and validated before the present work in steady-state conditions. The main innovation of this work resides in the integration of all these sub-models in a single tool and its adaptation and validation to speed and load transient conditions. Moreover, the tool can be run in PCs with Windows and UNIX operative systems, thus widening the possibilities to be used in powerful PCs.

## Virtual Engine Model (VEMOD)

The models presented in this paper are integrated into a gas dynamics software so-called VEMOD, which has been developed at CMT-Motores Térmicos. This computational tool arises as a response to highly limiting requirements of emission standards imposed by new homologation procedures, closer to real-world driving conditions in terms of engine dynamic operation, ambient temperature and altitude concerns. Current context demands the support of new computational tools able to accurately predict engine performance and emissions while reducing the cost of expensive tests campaigns usually based on chassis dyno calibration and road validation.

As shown in Figure 1, VEMOD fulfills these objectives based on an engine model covering the calculation of the different processes.

Firstly, the air management is computed by means of a 1D gas dynamics model which performs the calculations of the flow properties along the intake and exhaust systems as well as the high and low pressure EGR paths. Thus, specific sub-models are considered for the boosting system, air-charge and EGR coolers, throttle valves, heat transfer including gas-to-wall heat exchange and wall temperature prediction, aftertreatment sub-models (DOC and DPF), etc. The gas dynamics model is coupled to a cylinder model that predicts the in-cylinder conditions based on the combustion process. Detailed heat

transfer model is used to obtain the heat rejection to the chamber walls while mechanical losses model allows obtaining the brake power. An emission sub-model is coupled to the combustion process to predict raw NOx, CO, HC, and soot emissions as a function of the engine operating conditions. A physical approach is used for NOx while empirical correlations have been developed to predict CO, HC and soot. Different exhaust aftertreatment systems, such as DOC, DPF and deNOx systems (i.e. LNT or SCR) can be considered. Aftertreatment sub-models combine thermo-and fluid-dynamic with chemical modelling in order to assess the tailpipe emissions. This whole set of sub-models make up the engine model, marked with a blue box in Figure 1.

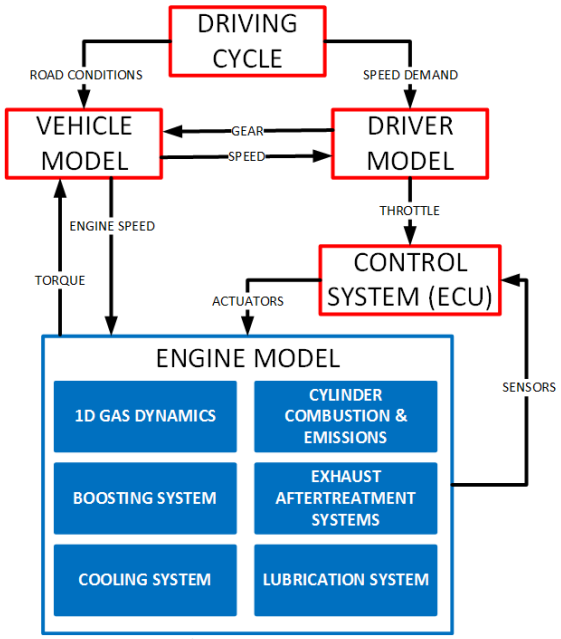

Figure 1. Flow-chart of Virtual Engine Model (VEMOD) modules.

The red boxes in Figure 1 represent the different control sub-models, which have been developed in Matlab/Simulink. They operate the engine model by actuating over the different actuators defined in the engine model. On one hand, a control system model emulates the electronic control unit (ECU) of the engine. ECU sets different engine actuators, as throttle position, EGR valves, VGT, etc., according to engine sensors information. In particular, throttle demand is imposed by the driving cycle being simulated. The vehicle model manages the vehicle response, which determines the engine speed as main input for the engine model. The results presented in this paper were obtained by operating the VEMOD through the Matlab/Simulink coupling. In the simulations performed, the VGT rack position and the EGR valves (low and high pressure) were controlled to reach the targets of intake pressure and fresh air mass flow respectively; the fuel mass injected was imposed.

VEMOD uses four different time scales to simulate the different engine processes. Gas dynamics and in-cylinder thermodynamics are calculated with a time-step which varies to ensure numerical stability, as later detailed. For reference purposes, a time-step of 0.01 ms can be given. Injection, combustion and emissions formation may require even smaller time steps. In such case, the current time step of the gas-dynamics model is divided into smaller parts. Thermal evolution of the engine block and the liquids is solved once per cycle (and thus time-step depends on the engine speed). Control system and vehicle model are executed with a fixed time step of 20 ms.

## *1D gas dynamics model*

The thermo-fluid dynamic model presented in this paper is able to reproduce the global behavior of a complete engine. Besides, it is able to calculate individually different components of the engine like the turbocharger, the heat exchangers, the cylinders or the aftertreatment systems, by means of specific sub-models.

In this model, the engine is based on 1D ducts and 0D elements such as the cylinders or the gas coolers. Along with the 1D ducts, the model solves the flow using the FVM [3] Godunov's method [4] and the HLLC Riemann solver [5, 6, 7]. The numerical technique is extremely conservative so big mesh size can be used to reduce computation time. All the relevant phenomena taking place along the duct are considered, this includes the wave interactions, which has an important effect on volumetric efficiency (especially in the intake/exhaust manifolds), the species transport (the thermodynamic properties of the gas depend on the composition and the temperature), the heat transfer between the gas and the duct walls (being possible to obtain the wall temperatures or imposing them) and the friction between gas and walls. Since the ducts are discretized in small cells, the conservation equations for mass, momentum and energy are solved at each cell at every time step. The Equation 1 shows the conservation equations system in its vector form for a given cell.

$$\frac{\partial \boldsymbol{W}_i}{\partial t} \cdot v_i + \left(-\boldsymbol{F}(\boldsymbol{W})_{i-\frac{1}{2}} \cdot A_{i-\frac{1}{2}} + \boldsymbol{F}(\boldsymbol{W})_{i+\frac{1}{2}} \cdot A_{i+\frac{1}{2}}\right) + \boldsymbol{V}_i \cdot \left(-A_{i-\frac{1}{2}} + A_{i-\frac{1}{2}}\right) + \boldsymbol{C}_i \cdot v_i = 0 \quad (1)$$

where:

$$\boldsymbol{W} = \begin{bmatrix} \rho \\ \rho \cdot u \\ \rho \cdot h_t \end{bmatrix}, \boldsymbol{F} = \begin{bmatrix} \rho \cdot u \\ \rho \cdot u^2 + p \\ \rho \cdot u \cdot h_t \end{bmatrix}, \boldsymbol{V} = \begin{bmatrix} 0 \\ -p \\ 0 \end{bmatrix}, \boldsymbol{C} = \begin{bmatrix} 0 \\ \rho \cdot G \\ -\rho \cdot q \end{bmatrix}$$

$$G = \frac{1}{2} \cdot u \cdot |u| \cdot f \cdot \frac{4}{D} \quad (2)$$

$G$ represents the fluid friction at the cell and $q$ is the heat transfer rate per unit mass.

It is known that the stability requirement for the calculation method limits the time step depending on the mesh size. Thus, the use of small ducts in some parts of the engine reduces the speed of the calculation. For a defined mesh size, the time step is restricted by the CFL condition, whose mathematical expression is given by Equation 3:

$$\frac{\Delta t}{\Delta x} \cdot |u - a| < C \quad (3)$$

Where $\Delta t$ is the time-step, $\Delta x$ is the mesh size, $u$ is the gas velocity, $a$ is the in-pipe speed of sound and $C$ is the Courant number (a value lower than 1.0 is required and 0.8 has been used). It defines a stability condition of numerical methods for hyperbolic equations such as the Euler equations governing the 1D flow in pipes.

In 0D elements, where a predominant flow direction does not exists (like in the cylinders or heat exchangers), the thermodynamic properties are considered homogeneous, and only the mass and energy balances are performed every time step.

Thus, the calculation method and the time-step independency between elements, result in an increase of the speed of calculation, which is about 10 times the real time.

Regarding the gases circuit of the tested engine, it has been implemented by means of pipes and volumes.

- Pipes length and diameter are set from the real values of the engine pipes. Mesh sizes are generally 30 mm; however, for pipes longer than 1 m, mesh size is 200 mm.
- The model contains 15 volumes: 4 represent the cylinders, 1 represents the compressor, another one represents the turbine, 3 volumes represent the different gas coolers (Intercooler, LP EGR cooler and HP EGR cooler), 1 volume represents the intake manifold, and another one volume represents the exhaust manifold. The four volumes left have been implemented for pipe joints.

## Boundary conditions

The different possible connections between elements have been modeled according to different boundary conditions to compute the flux between cells. Thus, for example, a valve is represented as a discharge coefficient between two elements. In 1D-0D connections, in order to compute the flux at the last cell interface, a virtual pipe is considered. It consist of the last cell connected from the pipe and another one with the properties of the 0D element (pressure, temperature and composition). 1D-1D connections are also computed by means of virtual pipes consisting of the cells that are directly connected. This connection can be used to join ducts with different diameters and different external cooling properties or flow restrictions. Multiple 1D-1D connections, like the one shown in Figure 2, require an auxiliary 0D element connected in the intersection of the multiple ducts in order to compute the flux at their outmost cells interfaces.

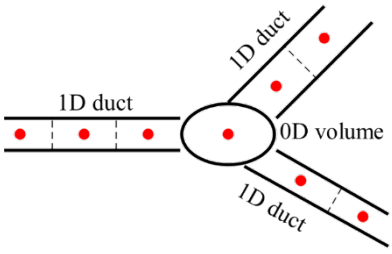


Figure 2. Multiple 1D-1D connection boundary.

## Heat transfer at pipes

The gas dynamics model calculates the internal heat transfer from the gas to the wall in each cell of the pipe at every time step as shown in Equation 4:

$$q_i = A_i \cdot h_i \left(T_g - T_{w,in}\right)_i \Delta t \qquad (4)$$

The gas temperature ($T_g$) is calculated every time step, while the inner wall temperature ($T_{w,in}$) is updated by mean of a simple conductance-capacitance model every engine cycle. For the calculation, the external heat transfer and the wall thermal inertia are taken into account.

In order to obtain the internal heat transfer coefficients at each cell, different correlations are used depending on the pipe type. Thus, under this approach, pipes are divided into intake or exhaust pipes, and intake or exhaust ports [8, 9, 10]. In a similar way, the external heat transfer coefficient is calculated depending on the pipe type defined before and whether it is cooled by air or by water [11, 12].

As mentioned, the gas dynamics model is the core of the Virtual Engine Model and the rest of sub-models are linked with it. The Table 1 shows the interaction between the VEMOD sub-models and the different engine systems.

Table 1. VEMOD engine systems and sub-models relations.

| | | FLUID CIRCUITS | | |
|---|---|---|---|---|
| | | **Gas circuit** | **Coolant circuit** | **Oil circuit** |
| **ENGINE SYSTEMS** | **Engine block** | • Combustion and emissions sub-model.<br>• Gas dynamics model.<br>• Heat transfer sub-model. | • Heat transfer sub-model.<br>• Hydraulic sub-model. | • Heat transfer sub-model.<br>• Hydraulic sub-model.<br>• Mechanical losses sub-model. |
| | **Turbocharger** | • Gas dynamics model.<br>• Heat transfer sub-model. | • Heat transfer sub-model.<br>• Hydraulic sub-model. | • Heat transfer sub-model.<br>• Hydraulic sub-model.<br>• Mechanical losses sub-model. |
| | **Coolers** | • Gas dynamics model.<br>• Heat transfer sub-model. | • Heat transfer sub-model.<br>• Hydraulic sub-model. | • Heat transfer sub-model.<br>• Hydraulic sub-model. |
| | **Pumps** | | • Heat transfer sub-model.<br>• Hydraulic sub-model.<br>• Mechanical losses sub-model. | • Heat transfer sub-model.<br>• Hydraulic sub-model.<br>• Mechanical losses sub-model. |
| | **Exhaust line** | • Gas dynamics model.<br>• Heat transfer sub-model.<br>• DOC and DPF sub-models | | |
| | **Ducts** | • Gas dynamics model.<br>• Heat transfer sub-model. | • Hydraulic sub-model. | • Hydraulic sub-model. |

## *Turbocharger sub-model*

The turbocharger is based on 0D compressor and turbine sub-models. They use the data provided by the supplier maps for both turbine [13] and compressor [14, 15] to compute the flow and the turbomachine efficiencies at any operating point within the maps. Besides, the model is able to extrapolate outside these maps so it is possible to simulate off-design conditions.

The extrapolation procedure for the reduced mass flow in the turbine [13] is based on modelling the turbine as a single equivalent nozzle. Thus, the equation of the throat area of the equivalent nozzle is deduced depending only on easy measurable geometry of the turbine, and on the available information in a standard map. The model is also able to extrapolate adiabatic efficiency. This extrapolation procedure is based on using the Euler equation of turbomachinery and assuming constant meridional component velocities.

The extrapolation procedure for the compressor ratio uses different mathematical approaches depending on the zone of the map (Low pressure ratio zone, low speed zone and high speed zone). This

compression ratio extrapolation model uses a generalized ellipse fitting approach developed by Leufven [16] for the low pressure ratio and high speed extrapolation. Additionally, for the low speed region, a model proposed by Martin et al. [17] is used, which is in turn a modification of the method of Jensen et al. [18]. It consists in keeping the coefficients of the Jensen's equation, tuned for the lowest measured speed line, for lower extrapolated speeds lines. For the compressor adiabatic efficiency a zonal approach was considered in order to adapt to different phenomena found beyond the usual compressor working conditions. Special attention was taken in the low speed extrapolation conditions, since it is the most critical zone because the compressor usually operates in this region at low engine loads.

The extrapolation procedure used in compressor and turbine requires the adiabatic efficiency. If the supplier maps were measured in non-adiabatic condition the model is able to remove the effect of heat on the efficiency by means of the heat transfer model. The heat transfer between the gas and the turbocharger, the heat transfer between the turbocharger housing and oil (or coolant if it exists) and with the ambient are calculated by a 1D lumped model [19]. The 1D lumped model connects several metal nodes that represents the parts of the turbocharger (turbine, compressor and housing) by means of conductive conductances. The convective heat between the walls and the different fluids is calculated by empirical correlations based in dimensionless numbers and fitted for several turbochargers. External heat [20] considers both convection and radiation.

The mechanical losses in the turbocharger shaft are also taken into account by modelling the shaft bearings friction. The model [21] is based on the Navier-Stokes equations applied to the two kinds of bearings (journal and thrust) normally used on this type of element. Making some assumptions, a simplified model for the two bearings has been obtained. The model takes into account the working point (turbocharger speed, oil temperature and axial force) and the geometrical characteristics of the bearings.

This model has been validated using engine load transients. In this tests the engine is stabilized at very low load and suddenly moves to full load. From the point of view of the turbocharger, the different parameters undergoes a lag due to its mechanical inertia. The results are also compared to those obtained using a turbocharger model based on maps. The main benefits of the turbocharger model included in the virtual engine are observed in turbine inlet and outlet temperatures, in particular in the turbine temperature drop predicted.

Figure 3 shows two load transients at different engine speeds. The experimental temperature was measured using a very low inertia transducer able to register transient evolution. The evolution of the turbine inlet and turbine outlet temperatures during the test has been compared for the experimental data, the results obtained using a typical map-based model and the results provided by the turbocharger model proposed for VEMOD. As can be observed, the use of a map-based model under predicts the temperature drop in the turbine. However, the use of a heat transfer model, as that included in the model proposed, improves the prediction of the turbine outlet temperature, very important for the operation of the after-treatment system placed downstream the turbine.

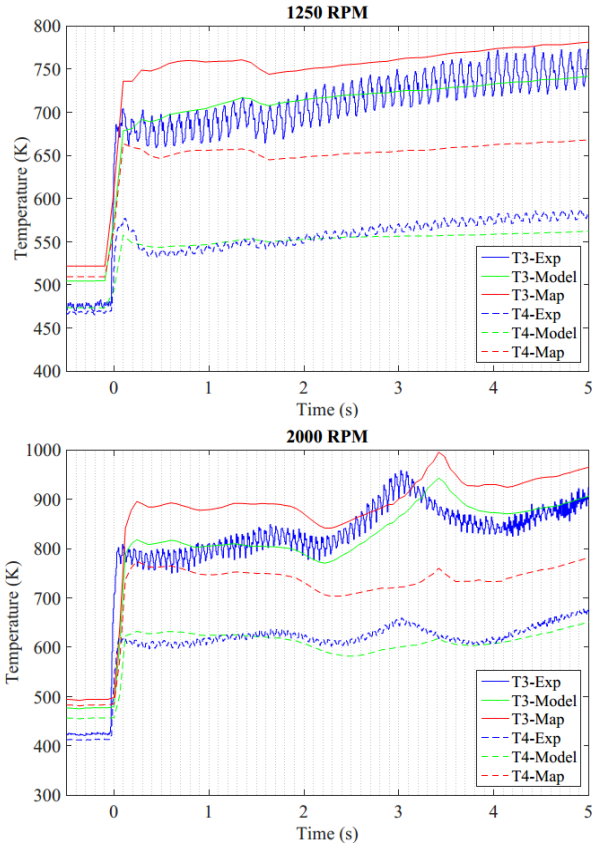

Figure 3. Turbine inlet and outlet temperatures during a load transient.

## *Injection, combustion and emissions sub-model*

The combustion and emissions sub-model consists of a 1D model able to predict the combustion profile and the main pollutant emissions with the required accuracy.

### Injection model

The main input for the combustion sub-model described in the next subsection is the injection rate. It is simulated by means of a semi-empirical model in which, starting from the injection settings (start of energizing time -SoE- and injected mass in each injection event) provided by the virtual ECU (later described), the injection rate is obtained. For each injection event the instantaneous injection rate is calculated assuming a simple shape composed of two or three straight lines (depending on whether the maximum needle lift is reached or not) representing the initial and final opening and closing transient processes, respectively, and a horizontal part representing the stationary maximum rate (if the complete needle opening is reached).

The model is based in four injector characteristics that are empirically obtained: the injector opening (A) and closing (C) times at maximum injection pressure, to reach maximum needle lift during the transient processes at the beginning and end of the injection event, the maximum injection rate (B) when the maximum needle lift is achieved, and finally, the hydraulic lag between the SoE and the start of the injection process (D). An experimental injector characterization campaign for different rail pressures and energizing times in an injector test rig following the methodology detailed in [22] allowed fitting empirical expressions for these four parameters as a function of the rail pressure. It is worth to remark that the maximum injection rate experimentally characterized as described, allows taking into account the dependency of the nozzle discharge coefficient with the injection pressure.

The model takes into account that for small injections (pilot and post injections) the stationary horizontal part of the injection will not be reached if the time for the complete needle opening is larger than the requirement for the injected mass of the event.

## Combustion model

A detailed description of the model can be found in [23]. For the shake of integrity, a short description is provided here. The combustion model is composed of three main sub-models: ignition delay, premix combustion and diffusion combustion models; along with a 1D model describing the mixing process.

The approach for the mixing process, key issue for both the heat release and emissions predictions, is a physical model based on the turbulent gas jet theory [23]. Even though it is not able to predict in detail the 3D spray behavior, the model allows evaluating the local conditions through the mixing model. It uses a double discretization of the combustion chamber (into two volumes corresponding to bowl and dead volume) and the spray (into a certain number of fuel elements). On the one hand, the bowl and dead volume have the same thermodynamic conditions (in fact their pressure and temperature is obtained by means of single zone 0D thermodynamic assumptions), but their composition is different once the combustion process has started. It is assumed that only the oxygen content of the bowl is available for the combustion process, and that the combustion products modify only the composition in the bowl. Later on, the composition of both regions is updated taking into account the mass exchange between them, which is governed by the evolution of the % of volume useful for combustion (this % of volume is the k-factor of the combustion chamber at TDC, and varies with the piston position). On the other hand, the composition and temperature of each fuel parcel is updated through the mass and energy balances, taking into account the instantaneous entrained mass conditions and composition. Thus, each injected fuel parcel mixes with the entrained gases (the composition and temperature of which correspond to the instantaneous chamber conditions) and, due to the combustion and the pollutant formation processes, the fuel parcel species suffer chemical transformations and its composition change. The temperature of each parcel is calculated by means of its energy balance, considering the enthalpy flow of the entrained gas and assuming that the parcel combustion products formed reach the adiabatic temperature (it is calculated assuming n-heptane combustion starting from the temperature of the unburned mixture at the calculation step). Finally, the combustion products and pollutants formed during each calculation step in all the parcels will change the mean bowl composition (thus affecting the gas properties), and the total heat release will be an input for the energy balance of the chamber 0D model.

The ignition delay (ID) model is based on a simplification and parameterization of a complete n-heptane chemical kinetics description from [24]. From this information, the $ID_i$ ($i$ is the parcel) can be calculated as a function of the local instantaneous conditions of each element. For that, the Shell model, which tracks the Livengood-Wu integral [25] is used, thus he ignition of the parcel occurs when:

$$\int_{t=POI}^{t} K_{ID1} \cdot p^{K_{ID2}} \frac{1}{ID_i} = 1 \qquad (5)$$

where $p$ is the in-cylinder pressure, $POI$ is the point of injection of the parcel $i$ and $K_{ID1}$ and $K_{ID2}$ are constants of the ignition model that have to be adjusted. The model assumes that the active radicals leading to autoignition are cumulated up to reaching a critical concentration. Once this critical concentration is reached, autoignition takes place. The model takes into account the effects of the thermodynamic conditions (p, T) and the local composition (EGR and F/A ratio) of the parcel $i$. The start of combustion (SOC) is determined for the first element that reaches the autoignition conditions.

The premixed combustion model is an empirical model that determines that the premix combustion of an element $i$ occurs when:

$$1 = \int_{SOC}^{t_{burn}} K_{pmx1} \cdot Y_{O_{2cyl}}^{0.855} \cdot \frac{Fr_i}{\exp(Fr_i - 1)} \cdot \exp\left(\frac{-K_{pmx2}}{T_{cyl}}\right) \cdot n^{K_{pmx3}} \cdot p_{inj}^{K_{pmx4}} \cdot \rho_{cyl}^{K_{pmx5}} \cdot dt \qquad (6)$$

Where $Y_{O2,cyl}$ is the bowl oxygen mass fraction, $\rho_{cyl}$ is the air density in the bowl, $F_r$ is the element relative fuel/air equivalence ratio, $T_{cyl}$ is the bowl temperature, $n$ is the engine speed, $p_{inj}$ is the injection pressure and $K_{pmx1}$, $K_{pmx2}$, $K_{pmx3}$, $K_{pmx4}$ and $K_{pmx5}$ are premix burned mass model constants. This empirical expression is related to the propagation velocity of the premixed flame around the auto ignition point.

If the oxygen/fuel ratio is higher to the stoichiometric value it will be in a poor premix situation and the entire fuel element mass will be burned. In this situation, the bowl composition will be updated with the combustion products resulting from this combustion. If the oxygen/fuel ratio is lower than the stoichiometric value it will be in a rich premix situation. The fuel mass element will be burned in two stages: a rich premix combustion where the oxygen mass in the element determines the fuel mass that will be burned (and the rest of the fuel mass will remain unburned) and the diffusion combustion where the fuel mass remaining after rich premix combustion phase will be burned in the diffusion combustion phase.

Finally, the diffusion combustion phase is assumed to be mixing controlled: the fuel mass in each element will be burned when it reaches stoichiometric conditions, and the achievement of these conditions is determined by the mixing model.

## Pollutant emissions model

Different approaches have been adopted to predict the pollutants. On the one hand, a physicochemical model has been used to predict $NO_x$ [26]. On the other hand, for the other pollutants (soot, CO and, UHC), where the fundamentals are unclear and/or which are affected by too many local phenomena, an empirical approach has been followed.

For the $NO_x$ emissions model, all the relevant mechanisms for $NO_x$ formation and reduction are considered, including thermal or Zeldovich [27], prompt and via $N_2O$ and the reburning effect. The model is implemented in a computational efficient way by tabulated chemistry where the instantaneous NO production is computed as shown in Equation 7:

$$\frac{dY_{NO,i}}{dt} = K_{dY_{NO,i}} \cdot \frac{Y_{NO_{eq,i}} - Y_{NO_i}}{Y_{NO_{eq,i}}} \qquad (7)$$

Where $Y_{NO,i}$ y $Y_{NOeq,i}$ are the instantaneous NO concentration in the parcel $i$, and the corresponding concentration in equilibrium and $K_{dY_{NO,i}}$ is the model constant. Both $K_{dY_{NO,i}}$ and $Y_{NOeq,i}$ are tabulated as a function of p, T and oxygen excess.

For the other mentioned pollutants, is not possible to propose a physical model. However, the amount of these emissions is very relevant for some other than pollution purposes, such as the DPF soot loading, the heat released at the DOC, etc. Consequently a prediction based on empirical correlations is proposed, expressed as a function of the most suitable parameters.

The CO formation empirical model is represented by the Equation 8:

$$Y_{CO} = K \cdot F(Fr) \cdot F(SOC) \cdot Y_{O_{2IVC}}^{A} \cdot ID^{B} \quad (8)$$

Where *K*, *A* and *B* are fitting constants, *Fr* is the fuel air equivalence ratio, *SOC* is the start of combustion, $Y_{O_{2IVC}}$ is the oxygen mass fraction at intake valve closing point, and *ID* is the ignition delay.

The CO correlation was adjusted using experimental data from steady-state tests (these tests are described in the "Experimental validation" section). The results are presented in Figure 4.

Equation 9 defines the correlation for UHC pollutant formation:

$$Y_{HC} = K \cdot F(Fr) \cdot F(SOC) \cdot Y_{O_{2IVC}}^{A} \cdot ID^{B} \cdot IP^{C} \quad (9)$$

Where *C* is also a fitting constant coefficient and *IP* is the injection pressure. The results predicted by this model against the experimental ones are presented in Figure 5.

Finally, the correlation used to predict soot formation is given by Equation 10:

$$Y_{soot} = K \cdot Fr^{A} \cdot n^{B} \cdot Y_{O_{2IVC}}^{C} \cdot ID^{D} \cdot IP^{E} \cdot \rho_{ICV}^{F} \cdot (1 + G \cdot EOC) \quad (10)$$

Where *D*, *E*, *F* and *G* are constant coefficients, $\rho_{IVC}$ is the in-cylinder charge density at intake valve closing point, and *EOC* is the end of combustion point. Results for soot formation model fitting are shown in Figure 6.

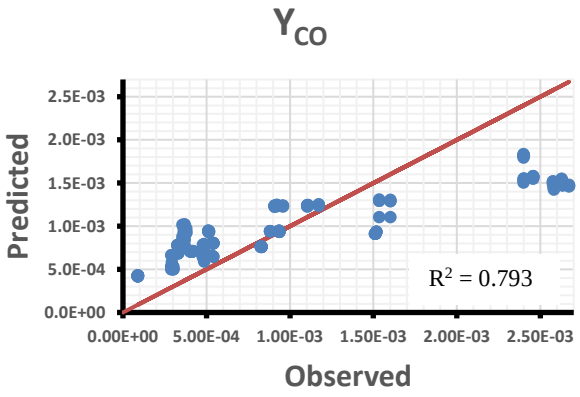


Figure 4. CO mass fraction, adjustment.

Finally, Figure 7 shows the modeled versus predicted NOx concentration.

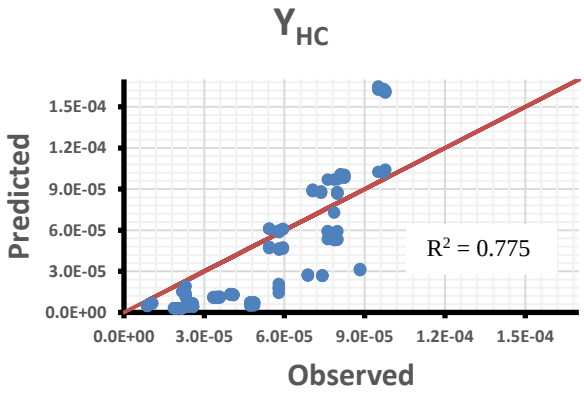


Figure 5. UHC mass fraction, adjustment.

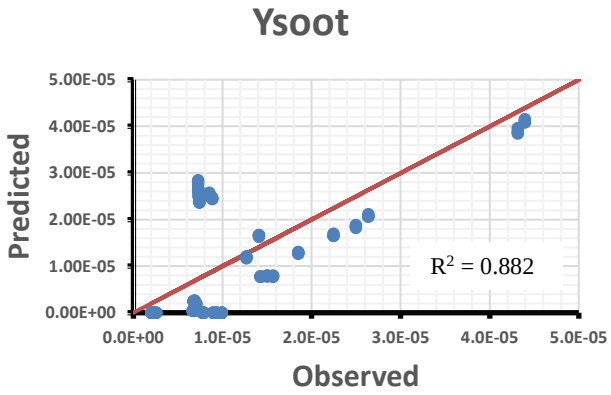


Figure 6. Soot mass fraction, adjustment.

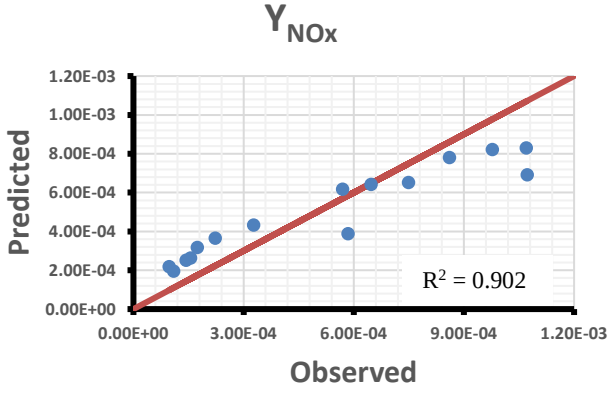


Figure 7. NOx mass fraction, adjustment.

The figures 4 to 7 correspond to a wide range of operating conditions covering most of the engine map. In them it is shown that there is a reasonably correlation between predicted values and experimental values, especially in the case on the NOx. There are slight discrepancies in CO, which is overpredicted at low concentrations and underpredicted at high CO level, and soot formation, which is also overpredicted but at high concentrations. In this case, the relative error for the soot formation is about 13.8%. The NOx predicted values match closely the observed ones for both low and high concentrations with a relative error of 3.8%.

### *In-cylinder heat transfer sub-model*

The in-cylinder heat transfer sub-model deals with the heat rejection in the combustion chamber and cylinder ports. This heat rejection is required in order to perform the energy balance in the combustion chamber and the global thermal balance of the engine block, which represents the most important heat source for the hydraulic circuit model.

In order to predict the heat rejection, a lumped conductance-capacitance model has been used [28, 29, 30]. This model allows linking in-cylinder and port processes with hydraulic circuits through the heat rejection calculation. This is achieved by dividing the cylinder head, the piston, and the cylinder into small metallic nodes. Each node has a characteristic mass and thermal capacitance depending on its geometrical and material properties. These nodes can be in contact with other metallic node so the conductive conductances are computed (e.g. piston-piston nodes) or in contact with fluid nodes, like the chamber, a coolant node or an oil node, obtaining the convective conductances instead.

The lumped model is initialized with geometrical information of the engine block (bore diameter, stroke, and ports diameters), the piston, the liner and the cylinder head materials, and the initial temperatures of the metallic nodes, oil and coolant. The nodes temperatures are then updated each cycle by applying a transient energy balance to each node.

Regarding the convection heat in the combustion chamber, a modified Woschni's correlation (Equation 11) has been used [31, 32] to obtain the heat transfer coefficient:

$$h_W = C_1 \cdot D^{-0.2} \cdot p^{0.8} \cdot T_g^{-0.53} \cdot \left(C_{W1} \cdot c_m + C_{W2} \cdot c_u + C_2 \frac{V \cdot T_{IVC}}{P_{IVC} \cdot V_{IVC}} (p - p_o)\right)^{0.8} \quad (11)$$

where $C_{W1}$, $C_{W2}$, $C_1$ and $C_2$ are tuned with empirical data from motored and firing tests [32], $c_m$ is the mean piston speed, $c_u$ is the instantaneous tangential velocity of the gas in the chamber, $p_0$ is the pressure in motoring conditions assuming a polytropic evolution, $p$ and $T_g$ are in-cylinder pressure and temperature, and $p_{IVC}$, $T_{IVC}$ and $V_{IVC}$ are pressure, temperature and volume at IVC, respectively.

### *Hydraulic circuits sub-model*

The hydraulic circuits sub-model allows calculating mass flow and temperatures of oil and coolant at different engine components like the engine block galleries, the EGR coolers, the turbocharger and the oil and coolant pumps. Hydraulic circuit elements like thermostats, operable valves, pumps and heat exchangers have been modeled and simulated. The process of creating the hydraulic circuit is flexible, due to the fact that it is made of generic components connected to each other. Then the user defines the specific properties (geometry, efficiency, pumps characteristic curves, etc.) for each component, just in the same way as the gas circuit.

The calculation method is the following:

1. First, starting from an arbitrary junction, all possible flow paths (open or closed) are found.
2. Paths are split at the junctions to find branches (a portion of a path between two consecutive junctions).
3. Closed paths are recognized as meshes, as shown in Figure 8.

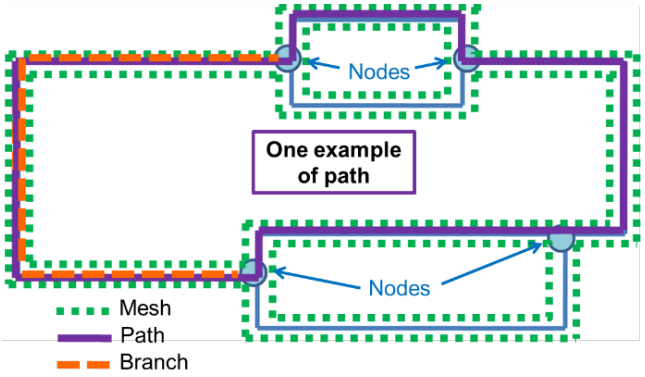


Figure 8. Distinction among path, branch and mesh in the hydraulic circuit.

4. For every branch, the head loss is obtained as a function of the flow in the branch:

$$H = h + R_1 \cdot \dot{V} + R_2 \cdot \dot{V}^2 \quad (12)$$

where $R_1$ and $R_2$ are hydraulic resistances and $\dot{V}$ is the volumetric flow. In the case of pipes, the hydraulic resistances are calculated with Darcy-Weisbach equation. Equation 12 is recalculated each engine cycle.

5. Finally, the network is solved by applying the Kirchhoff laws (mass balance for the junctions and energy balance for meshes). Thus, the flow through each branch and the pumps power are obtained.

The heat exchangers model works independently of the hydraulic circuit model, even though they use results from each other. Thus, the heat exchangers model needs the flow and the inlet fluid temperature from the hydraulic circuit, and it provides the heat rejection to calculate the fluid heating or cooling in the exchanger. The efficiency of each heat exchanger is calculated taking into account the type of heat exchanger (shell & tubes, crossflow…), the flow characteristics… Besides, it is possible to provide the model with a tabulated exchanger efficiency. Finally, the heat transferred is obtained by applying the NTU method. More information relating to the hydraulic circuits sub-model can be found in [33].

### *Mechanical losses sub-model*

The calculation of the mechanical losses is mandatory for accurate prediction of engine power, as shown in Equation 13.

$$N_b = N_i - N_p - N_{fr} - N_a \quad (13)$$

$$N_{fr} = N_{fr,piston} + N_{fr,bearings} + N_{fr,valvetrain}$$

$$N_a = N_{fuel} + N_{coolant} + N_{oil} \quad (14)$$

Where $N$ is power and subscripts $b$, $i$, $p$, $fr$ and $a$ stand for brake, indicated, pumping, friction and auxiliaries, respectively. It is important to note that indicated power and pumping losses are computed from the instantaneous in-cylinder pressure and volume calculated by means of the 0D in-cylinder sub-model included in the gas dynamic model. Thus, friction and auxiliaries losses have to be determined.

The model [31] considers two terms, on the one hand, the calculation of the friction due to engine elements with relative movement ($N_{fr}$).

Semi-empirical sub-models are used to calculate friction between piston pack and liner [34, 35], bearings [36, 37] and valvetrains [38, 39] considering the kinematics, dynamics and tribological processes of each element.

On the other hand, the calculation of the power required to drive the auxiliaries ($N_a$). Simple sub-models are used to determine the coolant, oil and fuel pumps power, taking into account information (flow and temperature) from hydraulic circuits and fuel pump characteristics.

To adjust the mechanical losses model, the total modeled losses are compared with the experimental ones (Equation 15):

$$\left(N_{fr}+N_a\right)_{exp}=\left(N_{fr}+N_a\right)_{mod}=k_{piston}\cdot N_{fr,piston}+$$

$$k_{bearings}\cdot N_{fr,bearings}+k_{valvetrain}\cdot N_{fr,valvetrain}+N_a \quad (15)$$

As experimental split of friction terms is not usually available, the calibration of the constants $k_{piston}$, $k_{bearings}$ and $k_{valvetrain}$ is performed simultaneously [31].

The Figure 9 shows the mechanical losses repartition in a 1.6 L DI Diesel engine. As observed, friction losses increase with both the engine speed and load, being the piston assembly the most important term except at very high speed, where the pumping becomes higher. The effect of the speed is justified taking into account the higher relative velocity of all the elements. The effect of the load is mainly observed in the piston pack friction due to the higher in-cylinder pressure that affects the rings friction. Valvetrain friction losses are the less significant.

Regarding auxiliaries losses, coolant pump losses increases significantly with the engine speed. Even though the fuel pump losses also increases with the engine speed, in this case the higher the load is the higher the losses are, due to the rail pressure.

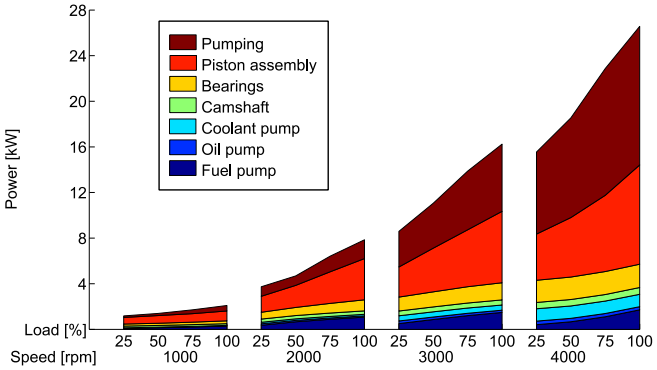

Figure 9. Mechanical losses distribution according to engine speed and load.

## *Aftertreatment sub-model*

The 1D gas dynamics model and the combustion and emissions sub-models set the boundary conditions to evaluate the performance of the different exhaust aftertreatment systems. In the case of a Diesel engine, DOC, DPF and deNOx systems. Aftertreatment sub-models combine thermo-and fluid dynamics with chemical modelling in order to assess the tailpipe emissions.

### DOC lumped model

The DOC model [40] deals with the main physical and chemical processes determining its performance in fluid-dynamic and emissions terms. The model is able to predict mass flow across the monolith, outlet gas temperature, outlet gas composition, i.e. pollutants conversion efficiency, as well as substrate and external canning wall temperature.

The DOC model consists of three sub-models solving pressure drop, heat transfer and chemical reactions based on a lumped quasi-steady approach. In VEMOD, the boundaries of all sub-models are defined by the gas dynamics model.

The installation of the DOC into the exhaust line imposes a flow restriction directly related to the geometry of the device and the flow inlet properties. Thus, the resulting pressure drop can be expressed as

$$\Delta p_{DOC}=\frac{1}{2}K_{DOC}\cdot\rho_{in}\cdot u_{in}^2 \quad (16)$$

where $K_{DOC}$ is the pressure drop coefficient of the DOC device, and $\rho_{in}$ and $u_{in}$ are inlet gas density and velocity.

The prediction of the outlet gas temperature is dependent on the heat exchange between inlet gas and substrate wall, whose temperature is in turn conditioned by the heat released by the chemical species conversion and the heat transfer towards the environment. The proposed lumped model accounts for these phenomena from a nodal-based scheme [41].

Regarding the reaction mechanism, the chemical reactions model predicts the HC and CO conversion efficiency. In the case of HC, besides oxidation, the modelling of their accumulation on a hydrocarbon adsorbent, typically a zeolite [42], during cold-start and warm-up periods is considered. The zeolite adsorbs hydrocarbons at low temperature keeping them trapped until reaching the desorption temperature.

### DPF model

The main features of the DPF model are the prediction of the fluid-dynamic behavior of the DPF canister and monolith in order to obtain the pressure drop along the system, the temperature prediction of the flow at DPF outlet and estimate the monolith and canister surface temperature, and the filtration and regeneration prediction within the system.

The pressure drop sub-model [43, 44] takes into account the pressure drop contributions in DPF monolith, which are the flow expansion at DPF monolith, the friction in inlet channel, the pressure drop in particulate layer, the pressure drop in porous wall, the friction in outlet channel and the flow diffusion at DPF monolith outlet. The inlet and outlet monolith boundary conditions (pressure, temperature and gas composition) are provided by the gas dynamics model, so that the DPF model determines the volumetric flow rate.

The heat transfer model is based on a nodal approach [41] where the heat transfer from gas to wall, the radial conduction, the convection and radiation to ambient, the axial conduction in canning, the heat released in soot oxidation and the monolith and canning thermal inertia are taken into account. By applying the energy balance and the continuity equation between monolith inlet and outlet, and taken into account the change in mass flow due to regeneration and filtration, it is possible to obtain the outlet gas properties.

The filtration model [45] computes the filtration efficiency and thus the amount of soot collected per unit cell, thus allowing to predict pressure drop during transient operations.

The regeneration model solves the mass conservation equation for the reagents in every layer and calculates the outlet mass fraction applying the stoichiometry of every reaction.

More information relating to the aftertreatment sub-model can be found in [46].

### *Vehicle, driver and control sub-model*

The flowchart of the vehicle, driver and control sub-model was shown in Figure 1. The control sub-model allows controlling the operating point of the engine model, both in steady-state points and during transient evolutions. The model is based on control algorithms built in Simulink which gather data from virtual sensors at determined positions of the VEMOD (intake air mass flow, boost pressure, engine brake torque, EGR mass flow, pressure and temperature at intake and exhaust manifolds, etc.) and operate over some actuators (VGT rack position, throttle valves lift, engine speed, injection pressure, and SOI and fuel mass of each pulse of injection). This way, the control model acts as a virtual ECU operating the engine. ECU calibration has been performed on the basis of experimental data obtained from engine steady-state tests. The engine operating map was discretized in order to have enough points to perform a reliable interpolation. The flexibility of the control sub-model allows the inclusion of corrections and different operation strategies such as EGR strategies for cold start and warm up processes.

The control model takes control of the injection by modifying the injection pressure, the fuel mass split ($m_{f1}$, $m_{f2}$, and $m_{f3}$) and the start of injection ($SOI_1$, $SOI_2$, and $SOI_3$) depending on engine speed and total fueling rate. The model also controls de air loop by means of the VGT rack position (which control is based on intake pressure set point, depending on engine speed and total fueling rate), and LP-EGR, HP-EGR and back pressure valves, which control is based on the air mass flow set point.

The vehicle control includes a clutch model represented by the following expressions:

$$\begin{cases} M_{clutch}(t) = M_{engine}(t) \; if \; M_{max}(t) \geq \left|M_{engine}(t)\right| \\ M_{clutch}(t) = M_{max}(t) \; if \; M_{max}(t) < \left|M_{engine}(t)\right| \end{cases}$$

$$M_{max}(t) = k(t) \cdot p_{max} \cdot S \cdot \mu_{clutch} \cdot r_{clutch} \qquad (17)$$

where $M$ stands for torque, $k(t)$ is a coupling ratio from 0 to 1 imposed by driver model, $p_{max}$ is the maximum coupling pressure and $S$, $\mu_{clutch}$ and $r_{clutch}$ are the contact area between friction discs, the disc friction coefficient and the average radius of the clutch disc, respectively. The clutch model distinguishes between clutch slip and no clutch slip situations. Another system that has been modeled is the gearbox, whose torque transferred to the transmission shaft is:

$$M_{gb} = k_{gb} \cdot r_{gb} \cdot M_{clutch}(t)$$

$$\begin{cases} k_{gb} = \eta_{gb}\left(T, gear, \omega_{gb_{in}}, |M_{clutch}|\right) \; if \; M_{clutch}(t) \geq 0 \\ k_{gb} = \frac{1}{\eta_{gb}\left(T, gear, \omega_{gb_{in}}, |M_{clutch}|\right)} \; if \; M_{clutch}(t) < 0 \end{cases} \qquad (18)$$

As shown in Equation 18, the gear box efficiencies can be expressed as a function of the gear, the operation temperature, the inlet shaft speed and the torque.

The vehicle dynamics model, which computes the instantaneous vehicle velocity, is fed with the gear box torque output and vehicle data such as vehicle mass and front area, wheel effective radius, gearbox shafts inertia, etc., and track information. The last one is important to take into account the track grade (vertical angle of the road to apply the force balance in the vehicle), the track radius (curvature radius of the track that affects the rolling resistance), and the wind speed and direction to calculate the aerodynamic resistance.

Finally, the driver model and logic consists of two parallel PID depending on active drive and logic.

It is important to note that the VEMOD can simulate any steady-state operating point without employing the control system sub-model, just by setting the target value of each actuator within the engine model. If a transient evolution is simulated, then the control system sub-model has to be used, but it can be run without making use of the vehicle model by setting the speed and torque.

## Experimental validation

The VEMOD has been validated experimentally in a HSDI Diesel engine. This is a 1.6L four-stroke engine compliant with Euro 5 emissions regulations whose specifications can be found in Table 2. From the point of view of thermal management, the low pressure EGR is cooled by a gas-coolant heat exchanger, and another gas-coolant heat exchanger cools the intake air to the cylinders. In order to reduce the warm-up time, the engine includes an electrovalve that blocks coolant flow through the engine block during engine warming.

Table 2. Engine specifications.

| | |
|---|---|
| Type | Euro 5 HSDI Diesel engine |
| Displacement | 1598 $cm^3$ |
| Stroke | 79.5 mm |
| Bore | 80 mm |
| Compression ratio | 14.5:1 |
| Number of valves | 4 per cylinder |
| Number of cylinders | 4 in line |
| Air management | VGT, LP-EGR, HP-EGR |
| Maximum power @ speed | 96 kW @ 4000 rpm |
| Maximum torque @ speed | 320 Nm @ 1750 rpm |

Table 3. Test cell instrumentation.

| **Variable** | **Instrument** | **Range** | **Accuracy** |
|---|---|---|---|
| Crank angle | Encoder | 0-360º | ±0.02 CAD |
| Torque | Dynamometer | 0-400 Nm | ±0.5 Nm |
| Gas/wall temperature | k-type thermocouple | 70-1520 K | ±2 K |
| Air mass flow | Sensyflow DN80 | 0-1700 kg/h | ±2 % |
| Coolant flow | Krohne 4010 Optiflux | 4.5-90 L/min | ±0.5% |
| Oil pressure | Piezoresistive transducer | 0-10 bar | ±25 mbar |
| In-cylinder pressure | AVL GH13P | 0-200 bar | Linearity 0.3% |

The test cell consists of a climate dynamic room, which allows performing cold start tests (up to -15ºC). The test cell is fully equipped to measure operation mean variables and in-cylinder pressures in the

four cylinders. It also includes a Horiba MEXA exhaust gas analyzer along with an AVL439 Opacimeter. Table 3 summarizes the relevant instruments used for this study. Data was acquired at a frequency of 10Hz with a test automation system.

Motoring tests were performed initially in order to adjust engine uncertainties and preliminary convective heat transfer tuning [32].

The engine combustion tests were performed in two stages. The first stage consisted of 26 steady-state points, some of them at cold start conditions (-7ºC). These points are specified in Table 4 and vary from low to high engine speed and from low to high load with the aim of covering a wide range of the engine map and testing points belonging the WLTP cycle. Engine operating parameters were set according to the calibration included in the engine control unit (ECU). Three repetitions of every operating point were measured.

Table 4. Steady-state tests performed.

| **Engine speed (rpm)** | **Load (%)** |
|---|---|
| 850 | idle |
| 1000 | 21, 44, 66, 88 |
| 1250 | 13, 26, 50, 76, 100 |
| 1500 | 11, 25*, 50, 75*, 100 |
| 2500 | 25, 50, 75, 100 |
| 3500 | 25*, 50, 75, 100 |

* Both, hot and cold, tests were performed.

The second battery of combustion tests consisted of different Worldwide harmonized Light vehicles Test Cycles (WLTC) in order to evaluate the transient behavior of the model. The cycle was measured starting from hot, ambient and cold conditions. Table 5 summarizes the different engine temperatures at these conditions. Three repetitions of each WLTC were measured.

Table 5. WLTC tests performed.

| **Test conditions** | **Room temperature** | **Engine block temperature** | **Coolant temperature** | **Oil temperature** |
|---|---|---|---|---|
| Hot | 20 ºC | ≈ 80ºC | ≈ 80ºC | ≈ 85ºC |
| Ambient | 20 ºC | 20 ºC | 20 ºC | 20 ºC |
| Cold | -7 ºC | -7 ºC | -7 ºC | -7 ºC |

Regarding the simulations, both the steady-state points and the WLTC simulations were performed by imposing the experimental values of engine speed, fuel mass, SOE of each injection, fuel rail pressure, and air mass flow and boost pressure target at every instant.

## Results and discussion

### *Steady-state validation*

Regarding the performance of the in-cylinder sub-model, Figure 10 and Figure 11 shows modeled heat release and the in-cylinder pressure obtained with VEMOD and the experimental one obtained with CALMEC [32], a combustion diagnosis tool developed at CMT-Motores Térmicos. In both figures, dashed lines correspond to the model prediction (blue is the heat released and green the in-cylinder pressure) while the solid lines correspond to the experimental values. The four solid lines (red is heat release and green the in-cylinder pressure) represents the four cylinders and give an idea about the dispersion among them. Two different engine speeds have been plotted as an example, one at low engine speed (1250 rpm) in Figure 10 and one at high engine speed (3500 rpm) in Figure 11.

Both figures show a good global performance with a slightly slower combustion. At low load the prediction is not so accurate than at high load due to uncertainties such as the fuel repartition in each cylinder.

Regarding the cylinder pressure, it can be observed that the pressure is well predicted, although simulated peak values are slightly lower at high speed and load. This is explained because of a slight overestimation of the incomplete combustion (the peak pressure difference is higher when the modeled cumulated heat release is lower in comparison with the average experimental value) and the blow-by. Besides, Figure 10 and Figure 11 show that the combustion is well centered in all the cases.

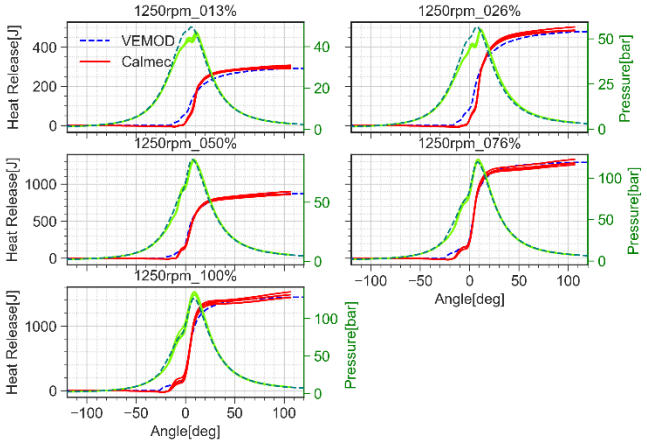


Figure 10. Cylinder heat release (J) at 1250 rpm for different loads (13%, 26%, 50%, 76% and 100%) in hot conditions.

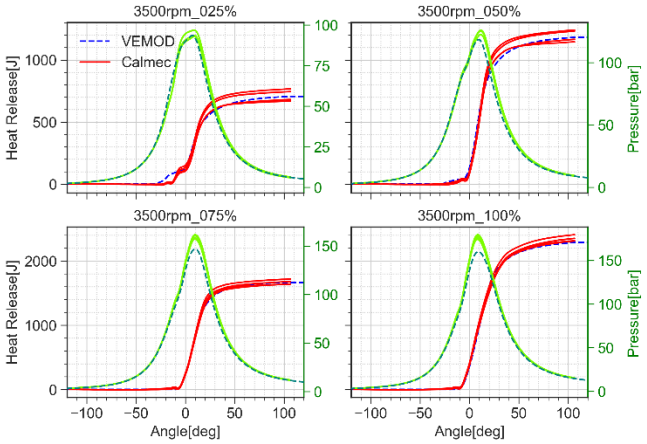


Figure 11. Cylinder heat release (J) at 3500 rpm for different loads (25%, 50%, 75% and 100%) in hot conditions.

It is interesting to note that the combustion model has no specific calibration parameter to take into account the operating conditions, but a constant in the diffusion sub-model and other five in the premixed model which are globally calibrated. As observed, except at low engine speed and load, the simulated heat release is in the experimental dispersion range between cylinders.

The in-cylinder peak pressure is shown in Figure 12. Here it is possible to see that at high speed and load, the predicted values are lower than the experimental ones. An explanation has been given when discussing Figure 10 and Figure 11: it is mainly due to a slight overestimation of the incomplete combustion at high load, where cylinder pressure is higher. Nevertheless, the absolute error is 2.73 bar, which means a 1.08% in relative terms.

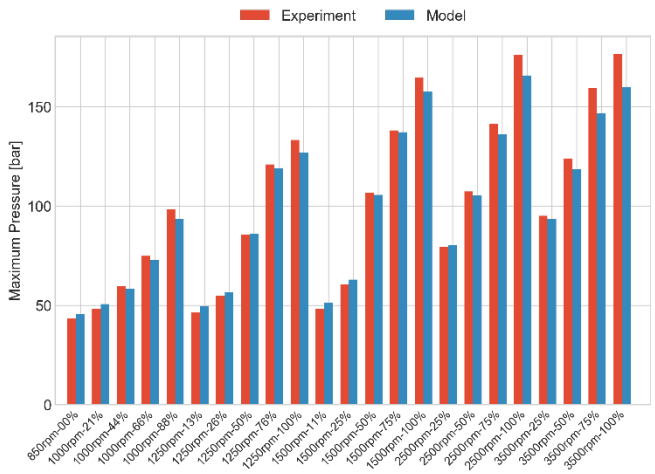


Figure 12. In-cylinder maximum pressure (bar) for each steady-state point in hot conditions. IMEP (bar) for each steady-state point in hot conditions.

IMEP for different simulated steady-state points are shown in Figure 13. They are well predicted, even though slightly underestimated, as consequence of the results of the modeled heat release and pressure shown. The absolute error is 0.38 bar, which means a 3% in relative terms.

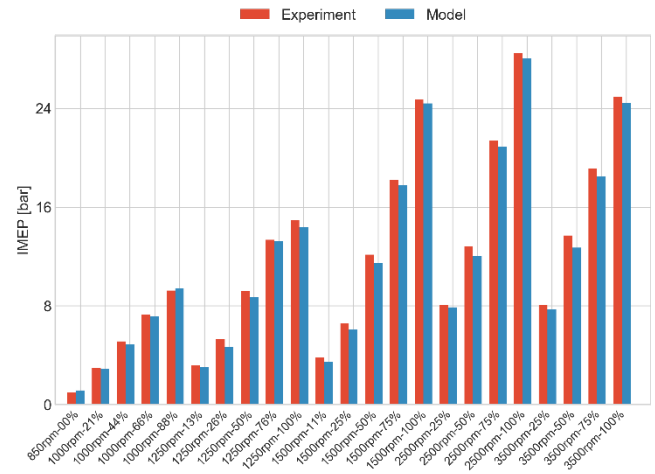


Figure 13. In-cylinder maximum pressure (bar) for each steady-state point in hot conditions.

Figure 14 and Figure 15 represents the average values of turbine outlet temperature and EGR rate for all the 23 steady-state points in hot conditions. Both figures show that the predicted values are quite accurate. Turbine outlet temperature presents a relative error equal to 2 %, meanwhile the EGR rate presents a mean error equal to 0.3 %.

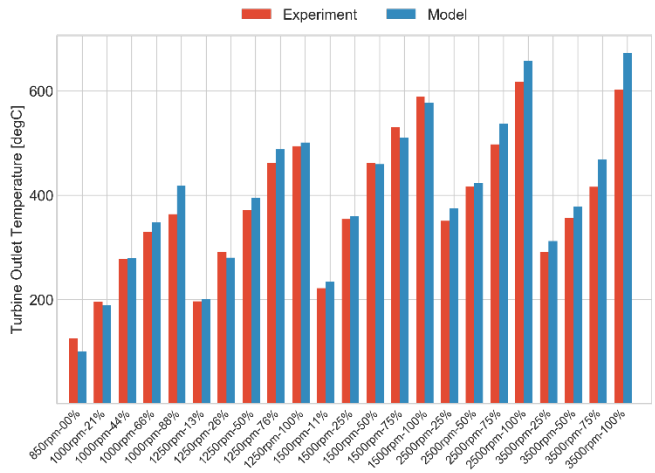


Figure 14. Turbine outlet temperature (ºC) for each steady-state point in hot conditions.

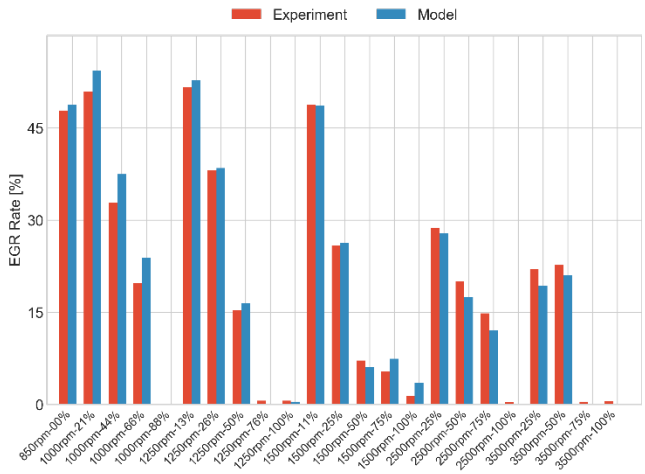


Figure 15. EGR rate (%) for each steady-state point in hot conditions.

The turbocharger speed, as well as the EGR rate, give an idea about the control sub-model accuracy, since it actuates over the VGT and LP EGR valve actuators. In this case, the relative error of the turbocharger speed is about 4 %.

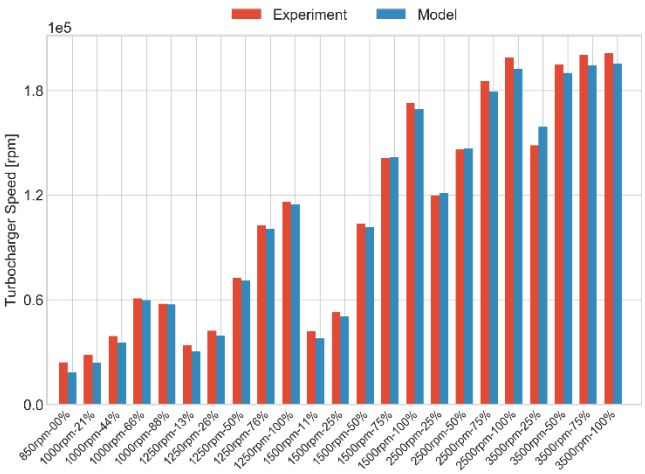


Figure 16. Turbocharger speed (rpm) for each steady-state point in hot conditions.

Figure 17 shows NOx mass flow for all the 23 steady-state points. As observed below, the NOx prediction model overestimates the NOx formation at high load and engine speed. The observed behavior is probably due to the intrinsic limitation of the model, thus it is clear that in the real chamber the composition and temperature of the gas is not homogeneous, however the model assumes that the entrained gas has the same properties for all the fuel parcels. This is probably the main uncertainty causing the observed trends. As the global calibration in the complete stationary map tries to reduce the differences in all the points, in some of them there is an overprediction while in other cases NOx are underestimated. As later observed in the transient validation, the weight of the different operating conditions during the WLTC is not the same as in the stationary points, thus appearing higher discrepancies at the end of the cycle, where higher loads are reached.

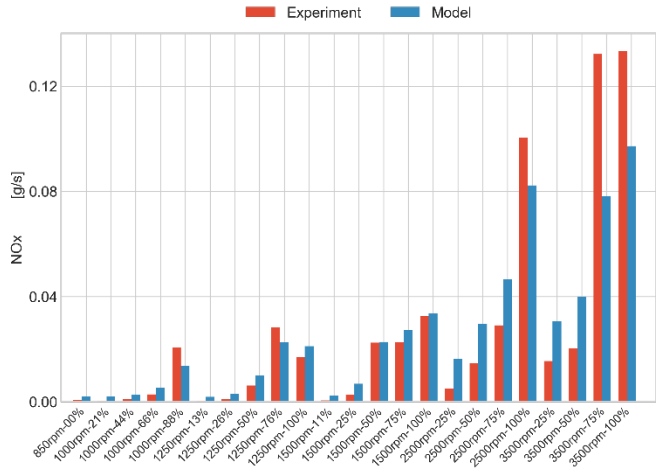


Figure 17. NOx mass flow (g/s) for each steady-state point in hot conditions.

## *Transient validation*

Regarding the simulation of the WLTC, it is not only interesting to evaluate the model prediction, but the model response to engine speed and load variations. Figure 18 and Figure 19 show the two controlled variables of the model, the air mass flow and the boost pressure, which are representative results to assess the accuracy of the control model. The air mass flow variations over time are well followed by the model, even though there are slightly higher experimental values at low load. This is probably due to the uncertainties in the compressor model at these low load conditions, where the experimental map is not available and the interpolation is performed. The same behavior is observed in the boost pressure. In this case the model values are higher at low load. This information is also presented in Figure 20 where it can be seen that there is less dispersion at high engine speed and load for both variables. The absolute mean error for the air mass flow is 0.21 g/s. During 90% of the time, the error is below 2 g/s. The absolute mean error for the boost pressure is 25 mbar and the error is below 29 mbar for 60 % of the points.

The zoomed parts of the WLTC show that model prediction and dynamics are quite accurate at high load and engine speed (both lines overlap each other) while minor discrepancies can be observed at low and medium engine speed, however the overall performance is good, as commented.

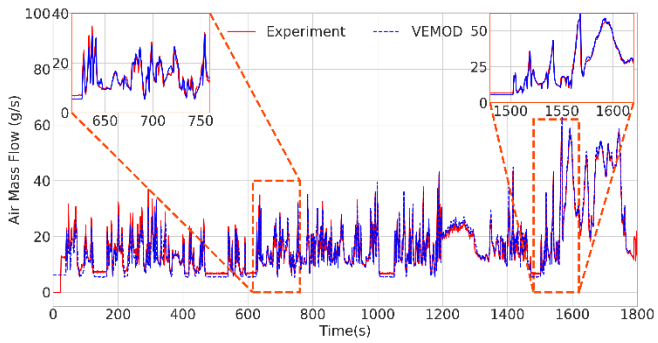


Figure 18. Air mass flow during WLTC at ambient conditions.

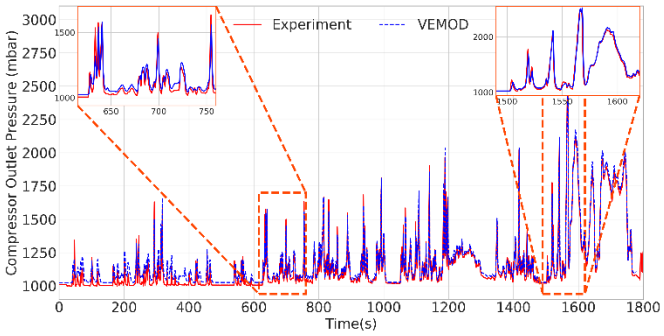


Figure 19. Boost pressure during WLTC at ambient conditions.

Note that points in Figure 20 are divided in 4 groups, according to the WLTC parts: low speed part (from 0 to 589 seconds), medium speed part (from 589 to 1022 seconds), high speed part (from 1022 to 1477 seconds) and extra high speed part (from 1477 to 1800 seconds).

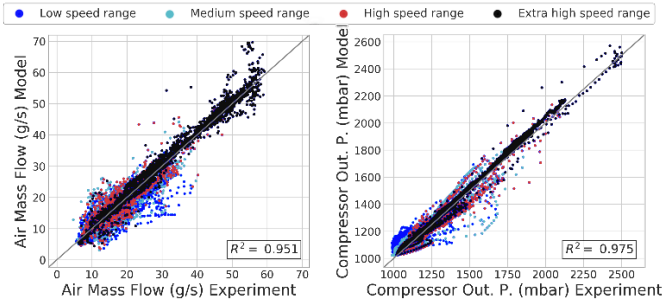


Figure 20. Air mass flow (left) and boost pressure (right). WLTC at ambient conditions.

Figure 21 shows that the torque variations over time are well followed. The prediction is pretty accurate, with a mean error of 3 Nm (2 %). Even though there are slightly higher model values at low load, the 90 % of the points present an error below 14 Nm. This can be observed in Figure 23, where the model fits best at high speed and load.

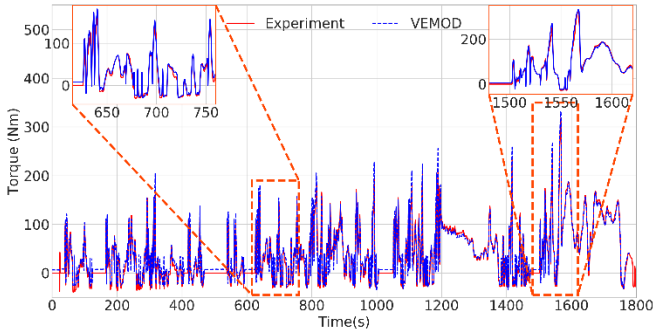


Figure 21. Brake torque during WLTC at ambient conditions.

Turbine outlet temperature, shown in Figure 22 shows a good model response to variations and, in general, with higher model peak values. The mean error for the turbine outlet temperature is 9 ºC (6 %) and the 60 % of the points present an error below 13 ºC. It is clear that the initial predicted turbine outlet temperature differs from the initial experimental value. This is mainly due to fact that the initial predicted temperature corresponds to the exhaust hot gases at the first simulated cycle, while the initial experimental temperature is the ambient one. Moreover, since the thermocouple has a determined thermal inertia, the instantaneous predicted temperature evolution (which is more responsive than the graphed one) has been filtered by applying a moving average, trying to reproduce the sensor behavior. However it seems that this simplification has to be improved, especially at the cycle beginning where the initialization is different.

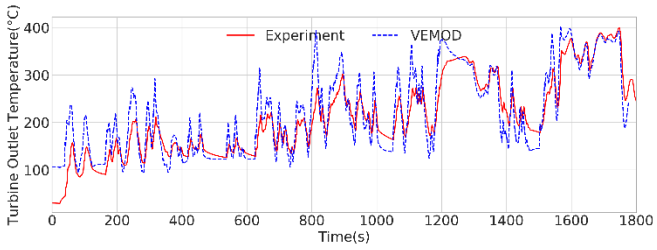


Figure 22. Turbine outlet temperature during WLTC at ambient conditions.

Figure 23 shows observed vs. predicted for torque and turbine outlet temperature during the WTLC. For the torque a correlation of 0.91 is obtained. In case of the turbine outlet temperature, even with the simple sensor behavior approximation used the correlation level is near 0.85.

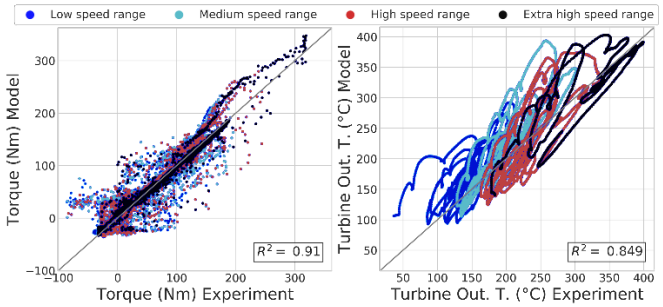


Figure 23. Torque (left) and turbine outlet temperature (right). WLTC at ambient conditions.

Regarding pollutant emissions, $CO_2$ variations are well followed and its prediction is pretty accurate as shown in Figure 24. As observed in Figure 24 (bottom), the predicted $CO_2$ accumulated mass fits well the real behavior, although the model overestimates the $CO_2$ production during the first part of the WLTC (low load and speed) and underestimates it at the end (high load and speed). Nevertheless, the mean error is 0.04 g/s and, during 80 % of the time, the error is below 0.44 g/s.

By contrast, $NO_x$ prediction is not so accurate. Figure 25 reveals that the $NO_x$ production is overestimated at high engine speed and load. This can be best observed on Figure 25 (bottom) where accumulated $NO_x$ mass is clearly higher at the end of the cycle. In this case, the mean error is 0.001 g/s (14%), while the maximum error is 0.025 g/s. The rest of pollutants are in general overestimated.

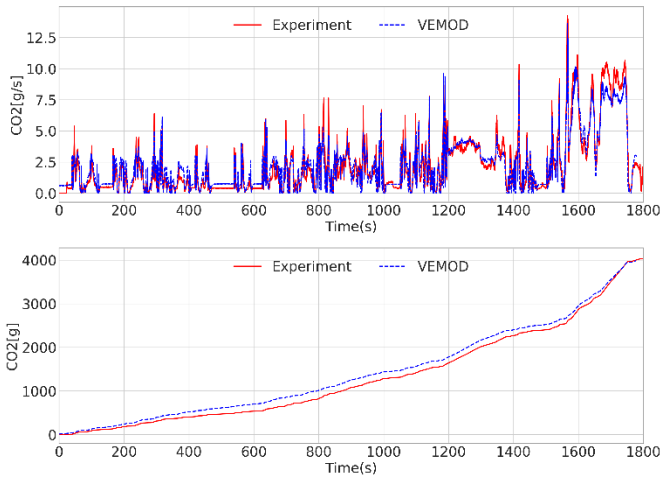


Figure 24. $CO_2$ mass flow (top) and $CO_2$ accumulated mass (bottom) over WLTC cycle at ambient conditions.

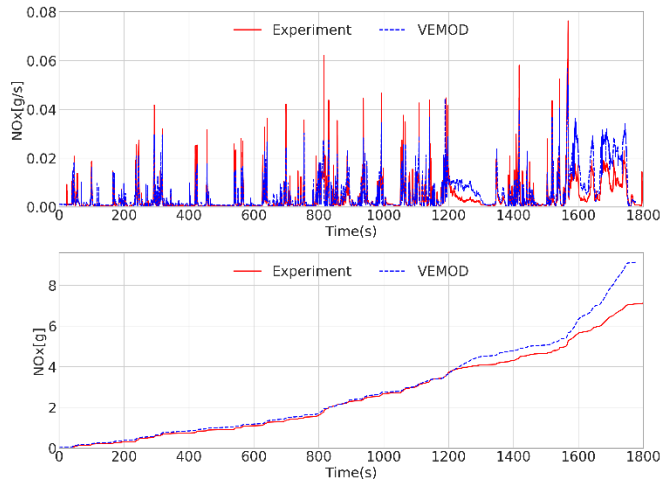


Figure 25. NOx mass flow (top) and NOx accumulated mass (bottom) over WLTC at ambient conditions.

## Summary and conclusions

A new Virtual Engine Model (VEMOD) has been presented. It is implemented as a standalone software tool and coupled with Matlab/Simulink to simulate real driving cycle tests. VEMOD and its sub-models workflow and characteristics were thoroughly explained. An extensive experimental campaign was conducted to accomplish the validation goals. Experimental tests consisted of 26 operating points in steady-state conditions plus the WLTC test cycle. Steady-state tests allowed to evaluate model performance at different engine speeds and loads both in usual (20ºC) and in cold (-7ºC) environments. The WLTC

was aimed at checking the model under highly dynamic, transient conditions.

The VEMOD was able to predict the overall thermo-fluid dynamics phenomena along the engine, providing reliable results with acceptable precision in both stationary and transient simulations. However, some discrepancies, mainly at high load where identified in the case of the NOx and peak pressure in the stationary validation. Fortunately, it has been shown that they had limited impact on the prediction of torque and $NO_x$ during the WLTC, which were two of the main goals of the model. Thus, it has been shown that many variables were well predicted during WLTC in ambient conditions such as engine torque, whose relative error was 2 %, and turbine outlet temperature, whose relative error was 6 %. The cumulated $CO_2$ emissions were predicted with a good accuracy, however it has been observed that the model overestimates the $CO_2$ production during the first part of the WLTC and underestimates it at the end. Regarding the NOx, it has been shown that the WLTC cycle is well reproduced except at the last part (high load and speed) having a mean error of 14 %.

Future works will be focused on the improvements of some models to give a better prediction at cold start conditions, as well as the improvement of the pollutant emissions sub-model regarding CO, UHC, NO and soot.

## References


1. Regulation (EC) No 715/2007 of the European Parliament and of the Council of 20 June 2007 on type approval of motor vehicles with respect to emissions from light passenger and commercial vehicles (Euro 5 and Euro 6) and on access to vehicle repair and maintenance information, Official Journal of the European Union, June 2007.
2. Payri, F., Lopez, J., Pla, B., and Graciano Bustamante, D., "Assessing the Limits of Downsizing in Diesel Engines," SAE Technical Paper 2014-32-0128, 2014, doi: 10.4271/2014-32-0128.
3. R.J. Leveque. "Finite-volume methods for hyperbolic problems". Cambridge Texts in Applied Mathematics. Cambridge University Press (2002).
4. S.K. Godunov. "A difference scheme for numerical solution of discontinuous solution of hydrodynamic equations". Matematicheskii Sbornik 47 (1959). 271-306.
5. B. van Leer. "Towards the ultimate conservation difference scheme, V. A second order sequel to Godunov's method". Journal of Computational Physics 32 (1979) 101-136.
6. E.F. Toro, M Spruce, W. Speares. "Restoration of the contact surface in the HLL Riemann solver". Technical report. CoA 9204. Department of Aerospace Science, College of Aeronautics, Cranfield Institute of Technology (1992).
7. E.F. Toro, M. Spruce, W. Speares. "Restoration of the contact surface in the Harten-Lax-van Leer Riemann solver". Shock Waves 4 (1994) 25-34
8. Depcik C, Assanis D. "A universal heat transfer correlation for intake and exhaust flows in a spark-ignition internal combustion engine". University of Michigan. SAE 2002-01-0372. 2002.
9. Santos R. "Estudio del aprovechamiento de la energía de los gases de escape en motores diésel". Doctoral thesis. Universitat Politècnica de València. 1999. (Text in Spanish).
10. Reyes M. "Modelo de transferencia de calor para colectores de escape de motores alternativos". Doctoral Thesis. Universitat Politècnica de València. 1994. (Text in Spanish).
11. Churchill SW, Bernstein MA. "Correlating equation for forced convection from gases and liquids to a circular cylinder in crossflow". J. Heat Transfer, vol 99 pp 300-306. 1977.
12. Dolz, V. "Transmisión de calor en motores alternativos: Aplicación al aprovechamiento energético de los gases de escape". Doctoral Thesis. Universitat Politècnica de València. (Text in Spanish).
13. Serrano JR, Arnau FJ, Garcia-Cuevas LM, Dombrovsky A, Tartoussi H. "Development and validation of a radial turbine efficiency and mass flow model at design and off-design conditions". Energy Conversion and Management.
14. Galindo J, Navarro R, Garcia-Cuevas LM, Tarí D. "An approach for extrapolating turbocharger compression ratio maps for engine simulations". Mathematical Modelling in Engineering & Human Behaviour. 2015.
15. Galindo J, Tiseira A, Navarro R, Tarí D, Tartourssi H, Guilain S. "Compressor efficiency extrapolation for 0D-1D engine simulations". SAE Technical Paper 2016-01-0554.
16. Leufvén, O., "Modeling for control of centrifugal compressors," PhD thesis, Linköping University, 2013.
17. Martin, G., Talon, V., Higelin, P., Charlet, A. et al., "Implementing Turbomachinery Physics into Data Map-Based Turbocharger Models," *SAE Int. J. Engines* 2(1):211-229, 2009, doi:10.4271/2009-01-0310.
18. Jensen, J., Kristensen, A., Sorenson, S., Houbak, N. et al., "Mean Value Modeling of a Small Turbocharged Diesel Engine," SAE Technical Paper 910070, 1991, doi: 10.4271/910070.
19. Olmeda P., Dolz V., Arnau F.J., Reyes-Belmonte M.A., "Determination of heat flow inside turbochargers by means of a one dimensional lumped model". Mathematical and Computer Modelling 57 (2013) 1847 – 1852.
20. Payri F, Olmeda P, Arnau FJ, Dombrovsky A, Smith L. External heat losses in small turbochargers: Model and experiments. Energy 71 (2014) 534 – 546.
21. Serrano JR, Olmeda P, Tiseira A, García-Cuevas LM. Theoretical and experimental study of mechanical losses in automotive turbochargers. Energy 55 (2013) 888 – 898.
22. Payri, R.; Salvador, F. J.; Gimeno, J. & Bracho, G. A new methodology for correcting the signal cumulative phenomenon on injection rate measurements. Experimental Techniques, 2008, Vol. 32, pp. 46 - 49, doi: 10.1111/j.1747-1567.2007.00188.x
23. Jean Arrègle, J. Javier López, Jaime Martín, Elena M. Mocholí. "Development of a Mixing and Combustion Zero-Dimensional Model for Diesel Engines". SAE Technical Paper 2006-01-1382.
24. V. Hamosfakidis, R.D. Reitz, "Optimization of a hydrocarbon fuel ignition model for two single component surrogates of diesel fuel," Combustion and Flame 132, pp 433-450, 2003.
25. Livengood JC, Wu PC. "Correlation of autoignition phenomena in internal combustion engines and rapid compression machines," Symp Int Combust 1955; 5: 347–356.
26. Payri, F., Arrègle, J., López, J., and Mocholí, E., "Diesel NOx Modeling with a Reduction Mechanism for the Initial NOx Coming from EGR or Re-entrained Burned Gases," SAE Technical Paper 2008-01-1188, 2008, doi: 10.4271/2008-01-1188.
27. Y.A. Zeldovich, "The Oxidation of Nitrogen in Combustion and Explosions," Acta Physicochim. USSR 21: pp. 577-628, 1946.
28. J. Torregrosa, P. Olmeda, B. Degraeuwe, M. Reyes, "A concise wall temperature model for DI Diesel engines," Applied Thermal Engineering 26 (11-12) (2006) 1320–1327. 578.
29. A. J. Torregrosa, A. Broatch, P. Olmeda, and C. Romero, "Assessment of the Influence of Different Cooling System Configurations on Engine Warm-Up, Emissions and Fuel Consumption," International Journal of Automotive Technology, vol. 9, no. 4, pp. 447–458, 2008.
30. A. J. Torregrosa, A. Broatch, P. Olmeda, J. Martín, "A contribution to film coefficient estimation in piston cooling galleries," Experimental Thermal and Fluid Science 34 (2) (2010) 142–151. doi:10.1016/j.expthermflusci.2009.10.003.

31. Payri, F., Olmeda, P., Martin, J., and Carreño, R., "A New Tool to Perform Global Energy Balances in DI Diesel Engines," SAE Int. J. Engines 7(1):43-59, 2014, doi: 10.4271/2014-01-0665.
32. Benajes, J., Olmeda, P., Martín, J., Carreño, R., "A new methodology for uncertainties characterization in combustion diagnosis and thermodynamic modelling," In Applied Thermal Engineering, Volume 71, Issue 1, 2014, Pages 389-399, ISSN 1359-4311, doi:10.1016/j.applthermaleng.2014.07.010.
33. Broatch, A., Olmeda, P., Martín, J., Salvador-Iborra, J., "Development and Validation of a Submodel for Thermal Exchanges in the Hydraulic Circuits of a Global Engine Model". SAE Technical Paper 2018-01-0160, 2018.
34. Stanley R., Taraza D. and Henein N. "A Simplified Friction Model of the Piston Ring Assembly". SAE Technical Paper 1999-01-0974, 1999.
35. Taraza D. and Henein N. "Friction Losses in Multi-Cylinder Diesel Engines". SAE Technical Paper 2000-01-0921, 2000.
36. Ushijima K., Moteki K., Goto T. and Aoyama S. "A Study on Engine Bearing Performance Focusing on the Viscosity-Pressure Characteristic of the Lubricant and Housing Stiffness". SAE Technical Paper 961144, 1996.
37. Tian T. "Modeling the performance of the Piston Ring-Pack in internal combustion engines". Ph.D. Thesis, Massachusetts Institute of Technology, 1997.
38. Beloiu D. "Modeling and Analysis of Valve Train, Part I – Conventional Systems". SAE Technical paper 2010-01-1198, 2010.
39. Guo J., Zhang W. and Zou D. "Investigation of dynamic characteristics of a valve train system". Mechanism and Machine Theory, Vol. 46 no 12, pp. 1950-1969, dec 2011.
40. J. Martín, P. Piqueras, L.M. García-Cuevas, E.J. Sanchis, "Lumped DOC modelling approach for fluid-dynamic simulation under engine dynamic operation," EAEC 2017 15th European Automotive Congress, Leganés, Spain, 2017.
41. Galindo J., Serrano J.R., Piqueras P. and García-Afonso Ó., "Heat transfer modelling in honeycomb wall-flow particulate filters," Energy 43 (2012) 201-213.
42. Kim D.J., Kim J.W., Yie J.E. and Moon H., "Temperature-programmed adsorption and characteristics of honeycomb hydrocarbon adsorbers," Industrial and Engineering Chemistry Research 41(25) (2002) 6589-6592.
43. J.R. Serrano, F.J. Arnau, P. Piqueras, Ó. García-Afonso, "Packed bed of spherical particles approach for pressure drop prediction in wall-flow DPFs (diesel particulate filters) under soot loading conditions," Energy 58 (2013) 644-654
44. J.R. Serrano, H. Climent, P. Piqueras, E. Angiolini, "Analysis of fluid-dynamic guidelines in diesel particulate filter sizing for fuel consumption reduction in post-turbo and pre-turbo placement," Applied Energy 132 (2014) 507–523.
45. J.R. Serrano, H. Climent, P. Piqueras, E. Angiolini, "Filtration modelling in wall-flow particulate filters of low soot penetration thickness," Energy 112 (2016) 883-898
46. Payri, F., Arnau, F.J., Piqueras, P., Ruiz, M.J., "Lumped Flow-Through and Wall-Flow Monolithic Reactors Modelling for Real-Time Automotive Applications". SAE Technical Paper, 2018-01-0954, 2018.

## Contact Information

Dr. Jaime Martín Díaz
CMT-Motores Térmicos, Universitat Politècnica de València
Camí de Vera s/n, 46022 Valencia (Spain)
Phone: +34 963877650
jaimardi@mot.upv.es

Dr. Francisco José Arnau Martínez
CMT-Motores Térmicos, Universitat Politècnica de València
Camí de Vera s/n, 46022 Valencia (Spain)
Phone: +34 963877650
farnau@mot.upv.es

## Acknowledgments

This research has been partially funded by the European Union's Horizon 2020 Framework Programme for research, technological development and demonstration under grant agreement 723976 ("DiePeR") and by the Spanish government under the grant agreement TRA2017-89894-R. The authors wish to thank Renault SAS, especially P. Mallet and E. Gaïffas, for supporting this research.

## Definitions/Abbreviations

| | |
|---|---|
| **0D** | Zero-dimensional |
| **1D** | One-dimensional |
| **CFL** | Courant-Friedrich-Levy condition |
| **DOC** | Diesel Oxidation Catalyst |
| **DPF** | Diesel Particle Filter |
| **EGR** | Exhaust Gas Recirculation |
| **FVM** | Finite Volumes Method |
| **HLLC** | Harten-Lax-van Leer Contact |
| **HSDI** | High Speed Direct Injection |
| **IVC** | Intake Valve Closing instant |
| **NTU** | Number of Transfer Units |
| **VGT** | Variable Geometry Turbine |
| $\mathbf{A_{i-1/2}}$, $\mathbf{A_{i+1/2}}$ | Section area at cell interfaces |
| $\mathbf{C_i}$ | Source term due to friction and heat transfer at cell |
| **D** | Diameter |
| **f** | Pipe roughness |
| $\mathbf{F(W)_i}$ | Flux vector at cell interface |
| $\mathbf{h_i}$ | Convective heat transfer coefficient at cell i |
| $\mathbf{h_t}$ | Total enthalpy at cell |
| **p** | Gas pressure |
| **u** | Gas velocity |
| $\mathbf{V_i}$ | Source term due to cell section area change |

| | | | |
|---|---|---|---|
| $\mathbf{v_i}$ | Cell volume | $\mathbf{\Delta t}$ | Time step |
| $\mathbf{W_i}$ | Solution vector at cell | $\mathbf{\rho}$ | Gas density |